

A phase field model for high-speed impact based on the updated Lagrangian formulation

Shourong Hao^a, Yihao Chen^a, Jun-Bo Cheng^b, Yongxing Shen^{a,*}

^a University of Michigan – Shanghai Jiao Tong University Joint Institute, Shanghai Jiao Tong University, Shanghai, 200240, China

^b Laboratory of Computational Physics, Institute of Applied Physics and Computational Mathematics, Beijing 100094, China

ARTICLE INFO

Keywords:

Phase field approach to fracture
Updated Lagrangian formulation
Finite deformation
High speed impact
Intense shock waves

ABSTRACT

High-speed impact problems usually undergo a form of highly localized plastic deformation under high strain rate with intense shock waves. In this paper, we present a coupled phase field model to simulate fracture in these situations. Our model considers the dynamic finite deformation with both strain hardening and strain rate hardening by the Johnson–Cook plasticity model. In particular, the formulation is posed in an updated Lagrangian framework and the constitutive update is realized with a return-mapping algorithm. Considering the tension–compression asymmetry, a new history variable is developed to enforce the irreversibility condition of crack propagation. The effectiveness of the proposed method is validated with a numerical example of 45 steel impact experiment along with two numerical simulations of split Hopkinson bar experiments on concrete and aluminum alloy specimens, where strong shock waves are generated. Besides, the effect of a few parameters is studied, namely, the regularization length parameter, the energy release rate, the initial impact velocity, and parameters of the Johnson–Cook model. These show the correct trend in terms of the time and extent of crack propagation.

1. Introduction

High-speed loading, with intense shock waves, is a common loading in explosion, impact and other processes. In this case, a few microcracks are formed in the extensively deformed material caused by the strong shock waves, and this area is often the source of further damage and complete failure.

There are already numerical investigations on the high-speed impact. These methods can be classified into three categories: the particle-based methods, the explicit crack path methods, and the diffuse-crack methods. In the first category, Li et al. [1,2] used the meshfree Galerkin method to simulate the failure mode. As an example of the second category, Song et al. [3] proposed a dynamic crack model based on the extended finite element method using phantom nodes, and Teng et al. [4] adopted the ductile fracture locus developed by Bao and Wierzbicki [5] to simulate the fracture in the hat specimen. In the last category, Liu et al. [6] presented a state-based peridynamic model to study the failure mode.

The phase field approach to fracture also belongs to the third category. This method is a synonym of the regularized variational fracture theory by Bourdin et al. [7]. Compared with traditional numerical methods for fracture, the phase field approach uses a diffuse zone to indicate the location of the crack, and the crack positions do not need

to be explicitly tracked, which significantly reduces the computational cost. Moreover, there is no need to input additional criteria for crack initiation and bifurcation behaviors. However, high computational cost may result from a fine mesh for an accurate solution of the phase field. Recently, by adopting neural networks, new machine learning methods and algorithms are presented and applied to solve the phase field problems efficiently, such as Samaniego et al. [8] and Goswami et al. [9]. For an overall description of the state of the art of the phase field model for fracture, see the reviews of Ambati et al. [10], Wu et al. [11], Bourdin and Francfort [12], and Wick [13].

The phase field model has been extended to dynamic fracture. For example, based on infinitesimal deformation, Zhou et al. [14] implemented their phase field model by COMSOL, whereas Nguyen and Wu [15] combined the cohesive zone model with the phase field model. Besides, an explicit method considering adaptive sub-step scheme for the update of phase field was proposed by Ren et al. [16]. For a detailed evaluation of existing phase field models for dynamic fracture, see Mandal et al. [17].

Existing contributions on simulating high-speed impact by the phase field method can be classified into two families: The hypoelastic approach, which adopts an additive decomposition of the rate of deformation into elastic, plastic, and thermal parts, of which the elastic part

* Corresponding author.

E-mail address: yongxing.shen@sjtu.edu.cn (Y. Shen).

<https://doi.org/10.1016/j.finel.2021.103652>

Received 17 April 2021; Received in revised form 14 September 2021; Accepted 17 September 2021

Available online 1 November 2021

0168-874X/© 2021 Elsevier B.V. All rights reserved.

is merely computed as the difference of the total rate of deformation and the inelastic (plastic and thermal) rates of deformation; and the hyperelastic approach, which uses a multiplicative decomposition of the deformation gradient into elastic, plastic, and thermal deformation gradients, assuming that an intermediate stress-free configuration exists.

In the first family, Chu et al. [18] developed a unified thermo-elasto-viscoplastic phase field model. In their model, the critical energy release rate is allowed to vary with the stress triaxiality to distinguish the failure properties of tensile fracture and shear banding, which are two types of fracture mode under high-speed impact. By using an energy model which excludes the plastic dissipation energy before the damage evolution into the failure energy, the simulation is able to take in account the microstructure evolution in ductile failure. Wang et al. [19,20] used a thermo-elastic-plastic phase field model combined with the Johnson–Cook model to incorporate strain hardening, strain rate hardening, and thermal softening. Considering that the material behavior in the shear band differs from that of the whole structure, the authors used a pure shear test to calibrate the model parameters. In the hat specimen simulation, their model is able to capture the transient “hot spot” phenomenon, which agrees with experimental observation. The authors reported that the loading rate and material properties have significant influence on the number and spacing of shear bands, and thermal softening plays an important role in inducing the initial shear band, but contributes less to the formation compared with damage softening. The model agrees with the theoretical models in [21–23] and experimental results in [24,25].

However, hypoelastic models have their drawbacks. From Brepols et al. [26], hypoelastic models are usually not based on the free energy potential, therefore there may be energy dissipation in closed elastic cycle loading, depending on the selection of the objective rate. Besides, according to Simo and Hughes [27, Chapter 9] and McAuliffe and Waisman [28], the hypoelastic formulations are not compatible with hyperelasticity, the latter of which is closely related to plastic flow in crystal plasticity, and except the logarithmic rate, the hypoelastic models will not define an elastic material.

Within the second family, McAuliffe and Waisman [29,30] put forward a coupled finite deformation model considering thermo-viscoplasticity with strain hardening, strain rate hardening, thermal softening, and diffusive regularization. The fracture is modeled by the phase field method, and part of the plastic work is considered as one source of the fracture-driven energy. Their model can capture the failure transition when the sample was loaded in different velocities. Borden et al. [31] proposed a mechanism considering the stress triaxiality as a driving force of phase field. By the yield surface degradation function, they introduce a plastic softening mechanism and a correction for the behavior of elastic deformation after crack initiation. A distinct feature of [31] is the use of a cubic degradation function rather than the traditional quadratic one, and the former is able to describe the behavior before crack initiation, giving a nearly linear stress–strain relationship before reaching the critical stress, and allowing a coarser mesh. Ambati et al. [32] proposed a phase field model for ductile materials in three-dimensional finite strain setting. By introducing a scalar metric of the accumulated plastic strain, the authors set up a relation between the phase field degradation function and the said scalar value. The model can capture experimental observations such as necking in flat specimens and cup-cone fracture patterns in axisymmetric specimens.

In this paper, we put forward a new phase field model to simulate the fracture in finite deformation. The proposed model belongs to the second family, i.e., it is based on a similar multiplicative decomposition of deformation gradient. This model possesses a number of distinctive features. First, the overall framework is the updated Lagrangian formulation, whereas the majority of existing works seem to adopt the total Lagrangian formulation, the latter of which may experience difficulty in handling large mesh distortion. Under this updated Lagrangian framework, the governing equation of the phase field is

reformulated in the deformed configuration. Second, by adopting the Johnson–Cook plasticity model, both strain hardening and strain rate hardening are considered, for which the return mapping algorithm is applied to enforce the constitutive response. Third, a new history variable is developed considering the tension–compression asymmetry to enforce the irreversibility condition of crack propagation. Moreover, the displacement field is updated with an explicit algorithm while the phase field is solved with an implicit formulation, simultaneously ensuring the accuracy and efficiency.

This paper is organized as follows. The model is proposed in Section 2, which includes the kinematics, elastic, and plastic constitutive behaviors, phase field model and the conservation law. The discretization and numerical algorithms are introduced in Section 3. In Section 4, numerical experiments of impact tests and split Hopkinson bar tests will be presented, including validation with experimental results, parameter studies, and discussion. The conclusions will be given in Section 5.

2. Phase field model for elastic–plastic fracture at finite deformation

In this section, we will introduce the governing equations of the elastic–plastic fracture at finite deformation for the shock wave problems in details, based on a multiplicative decomposition of the deformation gradient. The governing equations include kinematics, constitutive models, and balance laws. For brevity, we only provide the updated Lagrangian formulation, which is more closely related to the constitutive update; we verified that the results of total Lagrangian and updated Lagrangian are almost identical, as expected.

2.1. Kinematics

Let $\Omega_0 \subset \mathbb{R}^n$, $n = 1, 2, 3$, be the reference configuration, i.e., the volume occupied by the solid at the initial time. For any $\mathbf{X} \in \Omega_0$, let $\mathbf{x} = \phi(\mathbf{X}, t)$ be the deformation mapping, where \mathbf{x} is the particle position at the current time t corresponding to \mathbf{X} . The displacement field is given by $\mathbf{u}(\mathbf{X}, t) = \mathbf{x}(\mathbf{X}, t) - \mathbf{X}$.

The deformation gradient \mathbf{F} is defined as

$$\mathbf{F} = \frac{\partial \mathbf{x}}{\partial \mathbf{X}} = \nabla_0 \mathbf{x} = \mathbf{I} + \nabla_0 \mathbf{u},$$

where \mathbf{I} is the second-order identity tensor, and ∇_0 represents the gradient operator associated with the domain at time 0.

Assuming a multiplicative decomposition into elastic and plastic parts, the deformation gradient \mathbf{F} can be written as

$$\mathbf{F} = \mathbf{F}^e \mathbf{F}^p, \quad (1)$$

where \mathbf{F}^e and \mathbf{F}^p represent the elastic and plastic deformation gradients, respectively.

In this work, we assume $\det \mathbf{F}^p \equiv 1$. As a consequence,

$$J = \det \mathbf{F}, \quad J^e = \det \mathbf{F}^e, \quad J = J^e.$$

Besides, the right and left Cauchy–Green deformation tensors are

$$\mathbf{C} = \mathbf{F}^T \mathbf{F}, \quad \mathbf{b} = \mathbf{F} \mathbf{F}^T,$$

respectively. We also define the elastic part of the left Cauchy–Green deformation tensor as

$$\mathbf{b}^e = \mathbf{F}^e \mathbf{F}^{eT}.$$

2.2. Elasto-plastic constitutive models

In this section, we will introduce the elastic and plastic constitutive equations under finite deformation based on the decomposition (1). Moreover, we will introduce the phase field $d \in [0, 1]$ as an internal variable to indicate the cracking state of material. The regions with $d = 0$ and with $d = 1$ are the pristine and fully broken states, respectively. Since the stiffness will become weaker as cracks form, the phase field will affect the constitutive relations.

2.2.1. Elastic constitutive relations

Elastic constitutive relations are closely related to the strain energy, which is a function of the elastic part of the deformation gradient.

For most materials, only tension but not compression will cause fracture. Therefore, we adopt a tension–compression decomposition of the strain energy density as

$$\Psi(\mathbf{F}^e, d) = g(d)\Psi^+(\mathbf{F}^e) + \Psi^-(\mathbf{F}^e),$$

where $g(d)$ is the degradation function, for which we adopt the form $g(d) = (1 - d)^2$. And Ψ^\pm takes the following form:

$$\Psi^+(\mathbf{F}^e) = \begin{cases} U(J^e) + \frac{\mu}{2} (\text{tr } \bar{\mathbf{b}}^e - 3), & \text{if } J^e > 1, \\ 0, & \text{if } J^e \leq 1, \end{cases}$$

$$\Psi^-(\mathbf{F}^e) = \begin{cases} 0, & \text{if } J^e > 1, \\ U(J^e) + \frac{\mu}{2} (\text{tr } \bar{\mathbf{b}}^e - 3), & \text{if } J^e \leq 1, \end{cases}$$

where

$$\bar{\mathbf{b}}^e = (J^e)^{-2/3} \mathbf{b}^e, \quad U(J^e) = \frac{\kappa}{2} \left(\frac{(J^e)^2 - 1}{2} - \ln J^e \right),$$

and $\kappa > 0$ and $\mu > 0$ are the bulk modulus and shear modulus of the material, respectively.

Then the Kirchhoff stress tensor $\boldsymbol{\tau}$ is given by

$$\boldsymbol{\tau} = -J^e p \mathbf{I} + \mathbf{s}, \quad \mathbf{s} = g(d)\mu \text{dev } \bar{\mathbf{b}}^e, \quad p = \begin{cases} -g(d)U'(J^e), & \text{if } J^e > 1, \\ -U'(J^e), & \text{if } J^e \leq 1, \end{cases}$$

where p is the hydrostatic pressure and \mathbf{s} is the deviatoric part of the Kirchhoff stress.

2.2.2. Plastic constitutive relations and flow rule

We adopt the Johnson–Cook plastic constitutive model [33] to take into account both strain hardening and strain rate hardening. Under the isothermal condition, the yield stress is expressed as

$$Y = (A + B(\epsilon^p)^N) \left(1 + C \ln \frac{\dot{\epsilon}^p}{\dot{\epsilon}_0^p} \right), \quad (2)$$

where A , B , C , and N are material parameters, ϵ^p and $\dot{\epsilon}^p$ are the equivalent plastic strain and plastic strain rate, and $\dot{\epsilon}_0^p$ is the reference plastic strain rate.

Combining the above model with the Huber–Mises plasticity flow theory, the yield condition is defined as

$$\mathbf{F}(\mathbf{s}, \epsilon^p, \dot{\epsilon}^p) = \|\mathbf{s}\| - \sqrt{\frac{2}{3}} Y,$$

where $\|\cdot\|$ is the Frobenius norm.

The flow rule is expressed by the Lie derivative as

$$\mathcal{L}\{\mathbf{b}^e\} = -\frac{2}{3} \gamma \text{tr}[\mathbf{b}^e] \mathbf{n}_s,$$

where γ is the plastic consistency parameter, and

$$\mathbf{n}_s := \frac{\mathbf{s}}{\|\mathbf{s}\|}, \quad \dot{\epsilon}^p = \sqrt{\frac{2}{3}} \gamma.$$

The Kuhn–Tucker loading/unloading conditions are

$$\gamma \geq 0, \quad f(\mathbf{s}, \epsilon^p, \dot{\epsilon}^p) \leq 0, \quad \gamma f(\mathbf{s}, \epsilon^p, \dot{\epsilon}^p) = 0.$$

And the persistency condition is given by

$$\gamma \dot{f}(\mathbf{s}, \epsilon^p, \dot{\epsilon}^p) = 0.$$

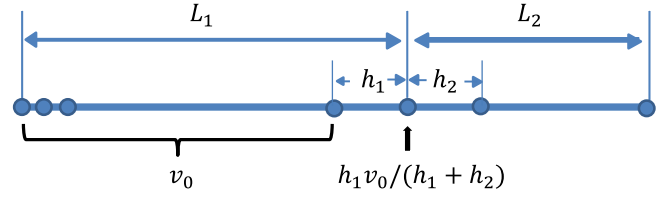


Fig. 1. The initial domain and initial discretized velocity of the 1D impact problem.

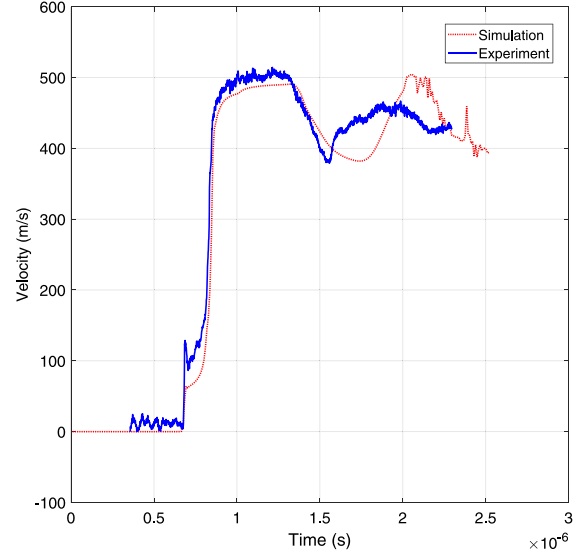


Fig. 2. Comparison of the right end velocity of simulation and experiment of 45 steel impact.

2.3. Phase field model

In this section, we set up the phase field model in the updated Lagrangian framework, and propose a new history variable to enforce the irreversible condition of crack growth.

In the total Lagrangian framework, the weak form for the phase field reads

$$-\int_{\Omega_0} \mathcal{H} \bar{d} \, d\Omega + \int_{\Omega_0} G_c \left(\frac{d\bar{d}}{\ell} + \ell \nabla_0 \bar{d} \cdot \nabla_0 \bar{d} \right) d\Omega = 0, \quad \forall \bar{d} \in H^1(\Omega_0) \cap L^\infty(\Omega_0),$$

where $G_c > 0$ is the critical fracture energy release rate, $\ell > 0$ is the phase field regularization parameter, and ∇_0 is the gradient operator associated with the initial domain.

Finally, \mathcal{H} is a history variable, which plays the role of $-g'(d)H$ for brittle fracture in Miehe et al. [34], with H a Miehe-style history variable. In this work, \mathcal{H} is specially reformulated to take into account the different fracture modes, which reads

$$\mathcal{H}(\mathbf{x}, t) = \max_{t' \in [0, t]} \{ -g'(d)\Psi^+[\mathbf{F}^e(t')] \} + W^p,$$

where W^p is a part of the plastic work contributing to the driving force for crack propagation, which is given by

$$W^p(t) = \int_0^t \text{Heav}(J^e - 1) \bar{\sigma} \dot{\epsilon}^p(t') dt',$$

and $\bar{\sigma} = \sqrt{\frac{3}{2} \mathbf{s} : \mathbf{s}}$ is the von Mises effective stress, and $\text{Heav}(\cdot)$ is the Heaviside function, to take into account the tension–compression asymmetry.

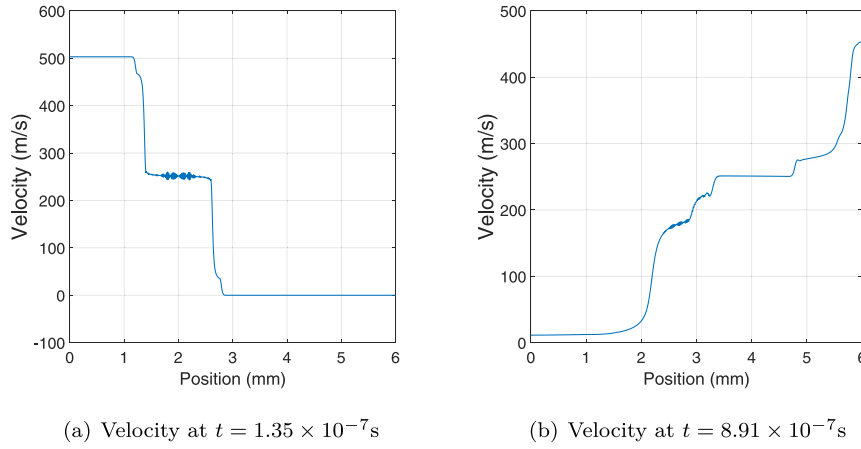


Fig. 3. Velocity as a function of the undeformed coordinate at different times.

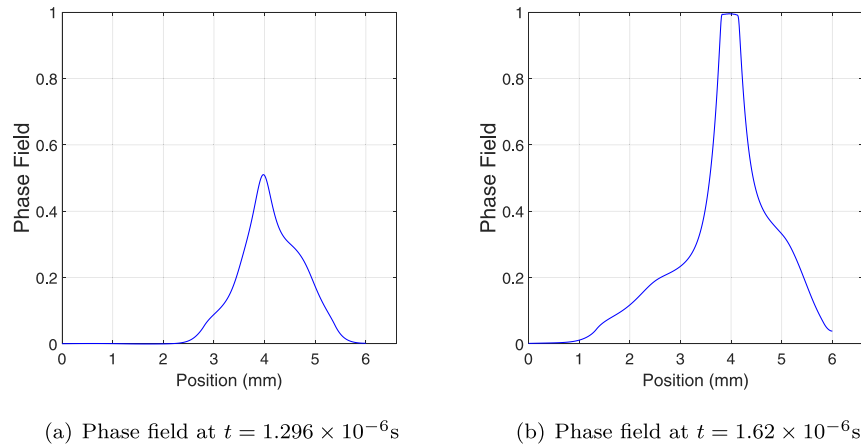


Fig. 4. Phase field growth during fracture.

Then by push-forward operations, the weak form in the updated Lagrangian framework becomes

$$-\int_{\Omega_k} \mathcal{H} \bar{d} J_k^{-1} d\Omega + \int_{\Omega_k} G_c \left(\frac{d\bar{d}}{\ell} + \ell \nabla_k d \cdot \mathbf{b}_k \nabla_k \bar{d} \right) J_k^{-1} d\Omega = 0, \quad \forall \bar{d} \in H^1(\Omega_k) \cap L^\infty(\Omega_k),$$

where ∇_k , $k \in \mathbb{N}$, is the gradient operator associated with step k (for time discretization, see Section 3.1) with $\nabla_k(\cdot) = \mathbf{F}_k^{-T} \nabla_0(\cdot)$, \mathbf{F}_k is the deformation gradient of step k relative to step 0, $J_k = \det \mathbf{F}_k$, and $\mathbf{b}_k = \mathbf{F}_k \mathbf{F}_k^T$.

Therefore, the corresponding boundary value problem for the phase field under updated Lagrangian reads

$$\begin{aligned} \frac{G_c}{\ell} [d - J_k \ell^2 \nabla_k (J_k^{-1} \mathbf{b}_k \nabla_k d)] &= H, & \text{in } \Omega_k, \\ \mathbf{n} \cdot \mathbf{b}_k \nabla_k d &= 0, & \text{on } \partial\Omega_k. \end{aligned}$$

2.4. Balance laws

In this part, we will introduce the balance laws.

The conservation of mass is

$$\rho J = \rho_0,$$

where ρ and ρ_0 are the mass densities in current and reference configurations, respectively.

The conservation of linear momentum is given by

$$\nabla \cdot \boldsymbol{\sigma} + \rho \mathbf{f}^b = \rho \mathbf{a},$$

where the Cauchy stress $\boldsymbol{\sigma}$ is related to the Kirchhoff stress $\boldsymbol{\tau}$ by

$$\boldsymbol{\sigma} = J^{-1} \boldsymbol{\tau} = -p \mathbf{I} + J^{-1} \mathbf{s},$$

\mathbf{f}^b is the body force per unit mass, and \mathbf{a} is the acceleration.

The displacement and stress fields are solved subjected to the following boundary conditions:

$$\mathbf{u} = \mathbf{u}_D, \quad \text{on } \partial_D \Omega_k,$$

$$\boldsymbol{\sigma} \cdot \mathbf{n} = \mathbf{t}, \quad \text{on } \partial_N \Omega_k,$$

where $\partial_D \Omega_k \cup \partial_N \Omega_k = \partial \Omega_k$, $\partial_D \Omega_k \cap \partial_N \Omega_k = \emptyset$.

2.5. Weak forms

In this subsection we provide the weak forms for the linear momentum balance and for the phase field evolution, which are the basis of the implementation.

For time step k , define $\mathbb{V}_k = \{\mathbf{u}(\cdot) \in H^1(\Omega_k; \mathbb{R}^n) | \mathbf{u} = \mathbf{u}_D \text{ on } \partial_D \Omega_k\}$. The weak form for the displacement is stated as: Find $\mathbf{u} \in \mathbb{V}_k$ such that

$$\int_{\Omega_k} \bar{\mathbf{u}} \cdot \rho \ddot{\mathbf{u}} d\Omega + \int_{\Omega_k} \boldsymbol{\sigma}(\mathbf{u}) : \boldsymbol{\varepsilon}(\bar{\mathbf{u}}) d\Omega = \int_{\Omega_k} \bar{\mathbf{u}} \cdot \rho \mathbf{f}^b d\Omega + \int_{\partial_N \Omega_k} \bar{\mathbf{u}} \cdot \mathbf{t} d\Gamma, \quad \forall \bar{\mathbf{u}} \in \mathbb{Z}, \quad (3)$$

where $\mathbb{Z} = \{\bar{\mathbf{u}} \in H^1(\Omega_k; \mathbb{R}^n) | \bar{\mathbf{u}} = 0 \text{ on } \partial_D \Omega_k\}$ and

$$\boldsymbol{\varepsilon}(\bar{\mathbf{u}}) = \frac{1}{2} [\nabla_k \bar{\mathbf{u}} + (\nabla_k \bar{\mathbf{u}})^T].$$

The weak form for the phase field is: Find $d \in H^1(\Omega_k) \cap L^\infty(\Omega_k)$ such that

$$-\int_{\Omega_k} \mathcal{H} \bar{d} J_k^{-1} d\Omega + \int_{\Omega_k} G_c \left(\frac{d\bar{d}}{\ell} + \ell \nabla_k d \cdot \mathbf{b}_k \nabla_k \bar{d} \right) J_k^{-1} d\Omega = 0, \\ \forall \bar{d} \in H^1(\Omega_k) \cap L^\infty(\Omega_k).$$

3. Discretization and numerical algorithms

In this section, we provide the discretization of the governing equations in spatial and temporal domains as used by the subsequent numerical examples.

3.1. Overall consideration

At the beginning, the initial domain Ω_0 is discretized into a quasi-uniform mesh of P_1 elements. In each time step, the displacement is updated using the standard central difference algorithm, followed by a constitutive update of the stress and plastic strain at each Gauss integration point and then an implicit solver of the phase field. Then the nodes of the mesh are updated according to the solved nodal displacements, giving rise to the updated domains $\Omega_1, \Omega_2, \dots$, where $\Omega_k, k \in \mathbb{N}$, is composed of all elements at time step k .

For Ω_k , the displacement field and phase field are discretized as

$$\mathbf{u}(\mathbf{x}) = \sum_{A=1}^{N_c} N_A(\mathbf{x}) \mathbf{u}_A, \quad d(\mathbf{x}) = \sum_{A=1}^{N_c} N_A(\mathbf{x}) d_A,$$

where N_c is the number of nodes, and $\mathbf{u}_A \in \mathbb{R}^n$ and $d_A \in \mathbb{R}$ are the displacement and phase field of node A , respectively. The collection of nodal values are denoted as \mathbf{u} and \mathbf{d} , when there is no risk of ambiguity.

Essentially what drives the change of the nodal displacements is the residual. According to (3), the component of the residual $\mathbf{R} = \mathbf{R}(\mathbf{u}, \mathbf{d})$ corresponding to node A is given by

$$\mathbf{R}_A = \int_{\Omega_k} \mathbf{B}_A^T \boldsymbol{\sigma}(\mathbf{u}) d\Omega - \int_{\Omega_k} \rho N_A \mathbf{f}^b d\Omega - \int_{\partial_N \Omega_k} N_A \mathbf{t} d\Gamma,$$

where \mathbf{B}_A is the strain–displacement matrix block associated with node A , whose size is 1×1 for 1D, 3×2 for 2D, and 6×3 for 3D, and here $\boldsymbol{\sigma}$ is expressed in Voigt's notation as a column vector. Besides, the classical lumped diagonal mass matrix \mathbf{M} is adopted for explicit solution.

Let the residual vector for \mathbf{d} be denoted \mathbf{R}_d . Then the component of \mathbf{R}_d corresponding to node A is given by

$$R_d^A = \int_{\Omega_k} -N_A \mathcal{H} J_k^{-1} d\Omega + \int_{\Omega_k} G_c \left(\frac{N_A d}{\ell} + \ell \nabla_k d \cdot \mathbf{b}_k \nabla_k N_A \right) J_k^{-1} d\Omega.$$

Both \mathbf{R} and \mathbf{R}_d can be obtained by a standard finite element assembly procedure. In each time step, the update of \mathbf{u} and \mathbf{d} is given in Algorithm 1.

3.2. Return mapping algorithm

Here we detail the constitutive update of the Johnson–Cook model (2), a rate-dependent model. The algorithm is based on [27, Chapter 9] for rate-independent models.

Compared with other models such as ideal plasticity or rate-independent models, the Johnson–Cook model has the feature that $\dot{\varepsilon}^p = 0$ implies $\sigma_y = -\infty$, which leads to $\mathcal{F}^{\text{trial}} > 0$, where $\mathcal{F}^{\text{trial}}$ is the yield function value for the elastic trial step. In other words, unless $\tau = 0$, plastic correction is always needed.

4. Numerical examples

In this section, three numerical experiments will be performed, that is, an impact experiment of a steel flyer on a plate, and two split Hopkinson bar experiments on concrete and aluminum alloy specimens. The evolution of velocity, phase field, and energy, the influence of parameters, the effect of mesh size, and the property of solver will be addressed in detail.

Algorithm 1: Update of displacement and phase field in $[t_k, t_{k+1}]$

Input: $\mathbf{u}_k, \mathbf{v}_k, \mathbf{a}_k, \mathbf{d}_k, \Delta t, \mathbf{M}$, tol
 // Input the displacement, velocity, acceleration, phase field at time k , and the time step, and tolerance
Output: $\mathbf{u}_{k+1}, \mathbf{v}_{k+1}, \mathbf{a}_{k+1}, \mathbf{d}_{k+1}$
 // Output the displacement, velocity, acceleration, and phase field at time $k+1$
1. Update the displacement;
 $\tilde{\mathbf{v}}_{k+\frac{1}{2}} = \mathbf{v}_k + \frac{1}{2} \Delta t \mathbf{a}_k$;
 $\mathbf{u}_{k+1} = \mathbf{u}_k + \Delta t \tilde{\mathbf{v}}_{k+\frac{1}{2}}$;
 Assemble $\mathbf{R} = \mathbf{R}(\mathbf{u}_{k+1}, \mathbf{d}_k)$, which involves Algorithm 2;
 $\mathbf{a}_{k+1} = -\mathbf{M}^{-1} \mathbf{R}$;
 $\mathbf{v}_{k+1} = \tilde{\mathbf{v}}_{k+\frac{1}{2}} + \frac{1}{2} \Delta t \mathbf{a}_{k+1}$;
2. Update the phase field;
 $\tilde{\mathbf{d}} = \mathbf{d}_k$;
 Assemble $\mathbf{R}_d(\mathbf{u}_{k+1}, \tilde{\mathbf{d}})$;
 // Newton–Raphson iteration
while $\|\mathbf{R}_d(\mathbf{u}_{k+1}, \tilde{\mathbf{d}})\| > \text{tol}$ **do**
 Assemble $\mathbf{K}_d = \mathbf{K}_d(\mathbf{u}_{k+1}, \tilde{\mathbf{d}})$;
 Solve $\Delta \mathbf{d}$ from $\mathbf{K}_d \Delta \mathbf{d} = -\mathbf{R}_d$;
 Update $\tilde{\mathbf{d}}$ by $\tilde{\mathbf{d}} = \tilde{\mathbf{d}} + \Delta \mathbf{d}$;
 Calculate $\mathbf{R}_d = \mathbf{R}_d(\mathbf{u}_{k+1}, \tilde{\mathbf{d}})$;
end
 $\mathbf{d}_{k+1} = \tilde{\mathbf{d}}$

4.1. The impact experiment of a steel flyer on a plate

First, we consider a 1D impact problem with strong shock waves as an example. Consider a very large plate $B_0^2 = (0, L_2)$ initially at rest. Its normal is along the x -direction. A flyer $B_0^1 = (-L_1, 0)$ collides B_0^2 completely inelastically along the normal direction at a velocity v_0 . Let the initial time $t = 0$ be the instant immediately after the impact, and the initial domain be $B_0 = B_0^1 \cup B_0^2$. The geometry is shown in Fig. 1.

We discretize the initial domain into equal-sized elements in B_0^1 and B_0^2 . The numerical value of the velocity of the merged point $X = 0$ is determined from the conservation of total momentum of the discrete system, which equals $h_1 v_0 / (h_1 + h_2)$, where h_1 and h_2 are the mesh sizes of the elements connected by the point $X = 0$. The discrete initial velocity is

$$v(X, t = 0) = \begin{cases} v_0, & X \in (-L_1, 0), \\ h_1 v_0 / (h_1 + h_2), & X = 0, \\ 0, & X \in (0, L_2). \end{cases}$$

Last but not least, both ends are free.

In this situation, the deformation gradient is simplified to

$$\mathbf{F} = \left(1 + \frac{du}{dX}\right) \mathbf{e}_x \otimes \mathbf{e}_x + \mathbf{e}_y \otimes \mathbf{e}_y + \mathbf{e}_z \otimes \mathbf{e}_z.$$

In the numerical implementation, the constitutive updating scheme is such that the input is the 3×3 deformation gradient \mathbf{F} and similar quantities. The parameters used are listed in Table 1.

In the sequel, we will first validate the simulation result with an experiment result. Secondly, we will examine the whole process of the impact problem and make some important observations. Finally, we will study the effect of a number of model parameters and compare the results with that of ideal plasticity.

Algorithm 2: Return mapping algorithm for the Johnson–Cook model**Input:** $\mathbf{u}_k, \mathbf{F}_k, \bar{\mathbf{b}}_k^e, \varepsilon_k^p, \mu$ // Input the (current iteration of) displacement, deformation gradient, equivalent plastic strain at time step k , and shear modulus**Output:** $\varepsilon_{k+1}^p, \bar{\mathbf{b}}_{k+1}^e, \boldsymbol{\tau}_{k+1}$ // Output the equivalent plastic strain, and Kirchhoff stress at time step $k+1$ **1. Compute the total and incremental deformation gradients;**

$$\mathbf{f}_{k+1} = \mathbf{I} + \nabla_k \mathbf{u}_k;$$

$$\mathbf{F}_{k+1} = \mathbf{f}_{k+1} \mathbf{F}_k;$$

2. Perform the predictor step;

$$\bar{\mathbf{f}}_{k+1} = [\det \mathbf{f}_{k+1}]^{-1/3} \mathbf{f}_{k+1};$$

$$\bar{\mathbf{b}}_{k+1}^{\text{trial}} = \bar{\mathbf{f}}_{k+1} \bar{\mathbf{b}}_k^e \bar{\mathbf{f}}_{k+1}^T;$$

$$\mathbf{s}_{k+1}^{\text{trial}} = \mu \operatorname{dev} [\bar{\mathbf{b}}_{k+1}^{\text{trial}}];$$

$$\varepsilon_{k+1}^p = \varepsilon_k^p;$$

3. Solve $g(\Delta\gamma) = 0$ by the Pegasus method [35];

where

$$g(\Delta\gamma) = \left\| \mathbf{s}_{k+1}^{\text{trial}} \right\| - 2\bar{\mu}\Delta\gamma - \sqrt{\frac{2}{3}} \left(A + B \left(\varepsilon_k^p + \sqrt{\frac{2}{3}} \Delta\gamma \right)^N \right) \left(1 + C \ln \frac{\sqrt{\frac{2}{3}} \Delta\gamma}{\varepsilon_0^p} \right)$$

$$\text{where } \bar{\mu} = \frac{1}{3} \operatorname{tr}(\bar{\mathbf{b}}_{k+1}^{\text{trial}}) \mu;$$

4. Perform the corrector step;

$$\mathbf{n}_s = \frac{\mathbf{s}_{k+1}^{\text{trial}}}{\left\| \mathbf{s}_{k+1}^{\text{trial}} \right\|};$$

$$\mathbf{s}_{k+1} = \mathbf{s}_{k+1}^{\text{trial}} - 2\bar{\mu}\Delta\gamma \mathbf{n}_s;$$

$$\varepsilon_{k+1}^p = \varepsilon_k^p + \sqrt{\frac{2}{3}} \Delta\gamma;$$

$$\bar{\mathbf{b}}_{k+1}^e = \bar{\mathbf{b}}_{k+1}^{\text{trial}} - \frac{2}{3} \Delta\gamma \operatorname{tr}(\bar{\mathbf{b}}_{k+1}^{\text{trial}}) \mathbf{n}_s;$$

5. Update the Kirchhoff stress;

$$\boldsymbol{\tau}_{k+1} = -J_{k+1} p_{k+1} \mathbf{I} + \mathbf{s}_{k+1};$$

$$\text{where } J_{k+1} = \det[\mathbf{F}_{k+1}], p_{k+1} = -U'(J_{k+1});$$

Table 1

Material properties and parameters in the steel flyer and plate experiment.

Parameter	Symbol	Value	Unit
Young's modulus	E	200	GPa
Poisson's ratio	ν	0.3	–
Mass density	ρ	7830	kg/m ³
Critical energy release rate	G_c	22	N/mm
Phase field regularized parameter	ℓ	0.15	mm
Mesh size	h	0.01	mm
Johnson–Cook parameter	A	496	MPa
Johnson–Cook parameter	B	434	MPa
Johnson–Cook parameter	C	0.07	–
Johnson–Cook parameter	N	0.307	–
Time step	Δt	9×10^{-10}	s

4.1.1. Validation with experimental results

We first perform a simulation with the parameters of 45 steel¹ to validate the simulation scheme with the experimental results of Hu et al. [36]. The geometric parameters and initial velocity are as follows: $L_1 = 2$ mm, $L_2 = 4$ mm and $v_0 = 503$ m/s. We set $\ell = 0.15$ mm and $h_1 = h_2 = 0.01$ mm, so the velocity of the merged point $X = 0$ is $v_0/2$. The other parameters are listed in Table 1.

Fig. 2 plots the right-end velocity of (1) our simulation and (2) experimental results in Hu et al. [36]. Our simulation result is in

¹ Terminology in the GB standard, corresponding to 1045 steel in the ANSI standard.

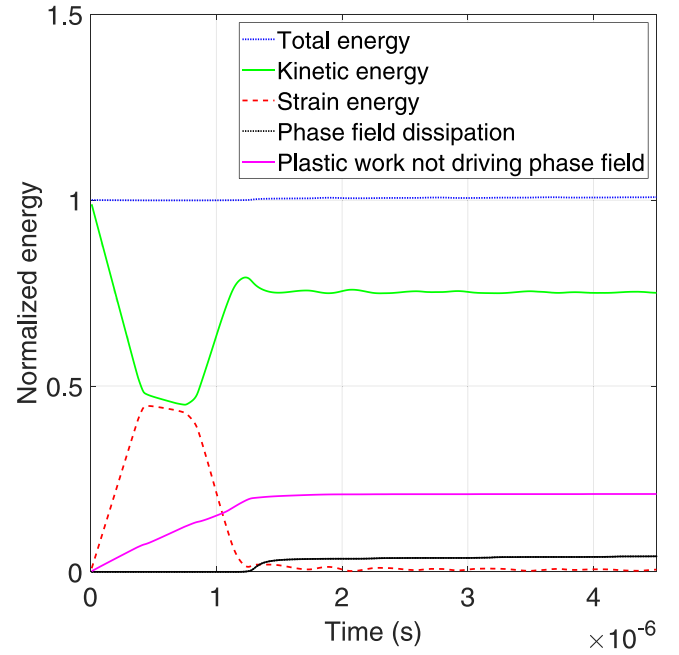


Fig. 5. The evolution of energies normalized by the initial total energy at $t = 0$. The normalized total energy almost maintains a value of unity over time.

excellent agreement with the experimental result all the way, especially before the wave caused by the fracture reaches the right free surface. After that, our simulation result predicts a tendency that the velocity decreases and then rises again, which is similar to the experimental results too.

4.1.2. Examining the whole process of the impact

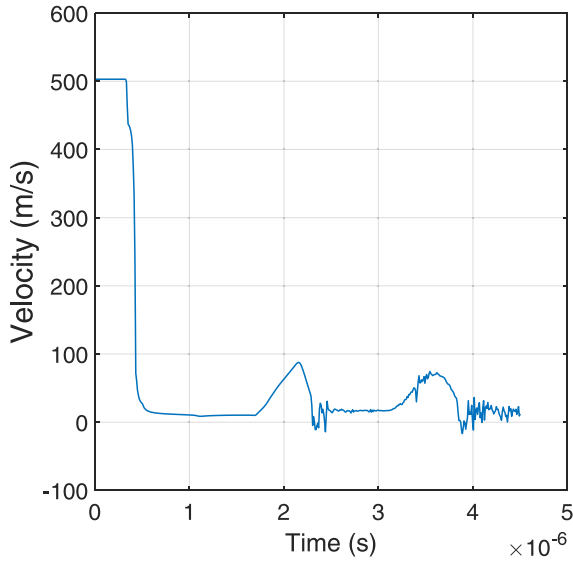
In this subsection, we examine the whole process of the impact problem. All parameters are the same as in the previous subsection. We set $h_1 = h_2 = 0.01$ mm, so the velocity of the merged point $X = 0$ is $v_0/2$.

Fig. 3 plots the velocity field as a function of the undeformed coordinate at $t = 1.35 \times 10^{-7}$ s and 8.91×10^{-7} s. Right after the collision corresponding to $t = 1.35 \times 10^{-7}$ s, two compression waves, one traveling to the left and the other to the right, are produced at the interface of the collision point $X = 0$. The wave traveling to the left decreases the velocity of nodes towards $v_0/2$ while the other one increases the velocity of nodes towards $v_0/2$. As a result, the element on the collision interface remains being compressed. As shown in Fig. 3, after reaching the boundary at $t = 8.91 \times 10^{-7}$ s, these two compression waves bounce back and become rarefaction waves. They continue to increase or decrease the velocity of nodes until they reach $v_0/2$. When the two waves meet for the first time after rebounding, a tensile stress area forms. The tensile stress in this numerical example is big enough to form a complete fracture.

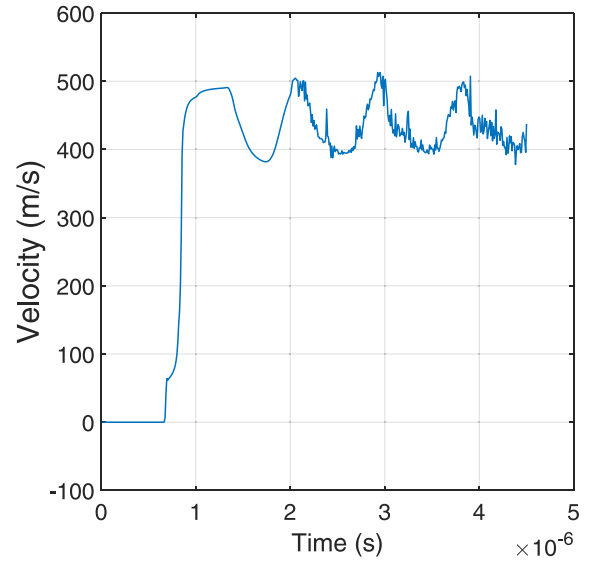
Fig. 4 plots the phase field as a function of the undeformed coordinate at $t = 1.296 \times 10^{-6}$ s and 1.62×10^{-6} s. From Fig. 4, the phase field in the region under tension constantly increases and finally reaches unity, indicating complete fracture at $t = 1.62 \times 10^{-6}$ s.

Fig. 5 plots the evolution of energies normalized by the initial total energy. The total energy includes strain energy, kinetic energy, phase field dissipation, and the part of plastic work not contributing to driving the phase field. From Fig. 5 we see that the total energy almost maintains to be unity, indicating that the total energy conserves.

Fig. 6 plots the velocity of the left and right ends. Before fracture, when the waves reach the end, the velocity of the left end reaches 0 and the velocity of the right end reaches v_0 in less than 4×10^{-7} s. After

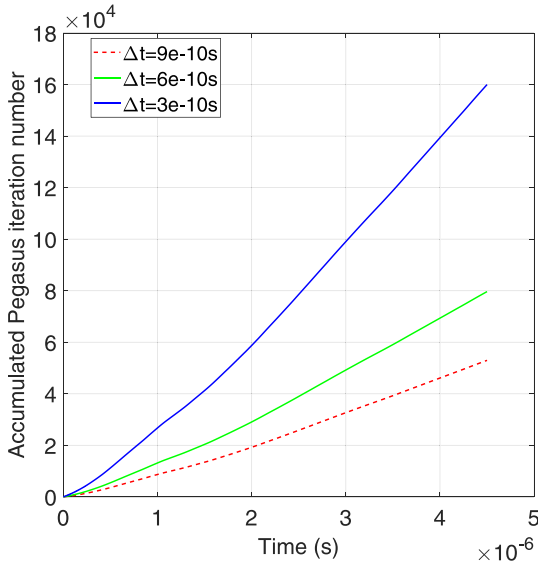


(a)



(b)

Fig. 6. Evolution of the velocity at the left end (a) and right end (b).

Fig. 7. Accumulated Pegasus iteration number averaged at each element as a function of time with different Δt 's. The accumulated Pegasus iteration number increases as Δt decreases.

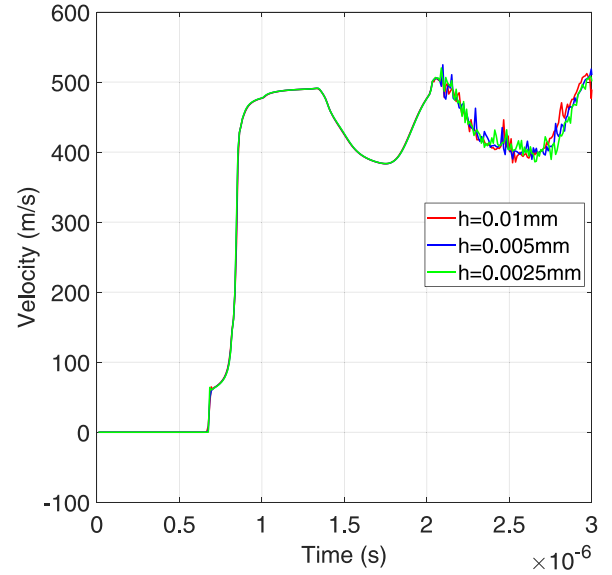
fracture, they decrease or increase and then restore the velocity of the end by the same amount. This process takes less than 1×10^{-6} s.

Fig. 7 plots the accumulated Pegasus iteration number averaged at each element as a function of time with different time step Δt 's. As Δt decreases, the accumulated Pegasus iteration number increases, which shows that a finer time step is more costly, as expected.

4.1.3. Parameter study

In this section, we will study the effect of different parameters, namely ℓ , G_c , v_0 , A , B , and C . The default parameters are given in Table 1.

Effect of the mesh size h . Fig. 8 plots the velocity of the right end with mesh size $h = 0.01$ mm, $h = 0.005$ mm, and $h = 0.0025$ mm, and the results show that they are almost the same. As a result, we regard

Fig. 8. Comparison of the right end velocity with mesh sizes $h = 0.01$ mm, $h = 0.005$ mm, and $h = 0.0025$ mm. The three curves show little difference prior to the onset of fracture, $t = 1.62 \times 10^{-6}$ s.

the mesh with $h = 0.01$ mm as sufficiently refined. The reason of the oscillations after $t = 2 \times 10^{-6}$ s may be attributed to the absence of dissipation mechanism after complete fracture ($t = 1.62 \times 10^{-6}$ s). Despite of this, energy is conserved, see Fig. 5.

Effect of the regularization length scale ℓ . To study the effect of ℓ , we change its value and keep $\ell/h = 5$, leaving the other parameters unchanged. We choose three values for ℓ : 0.025 mm, 0.05 mm, and 0.1 mm.

Fig. 9 plots the phase field as a function of the underformed coordinate X with different ℓ 's at $t = 1.62 \times 10^{-6}$ s. The time to complete fracture with different ℓ 's is the same, which is $t = 1.62 \times 10^{-6}$ s. The larger ℓ is, the larger the phase field at the same time and the same location is.

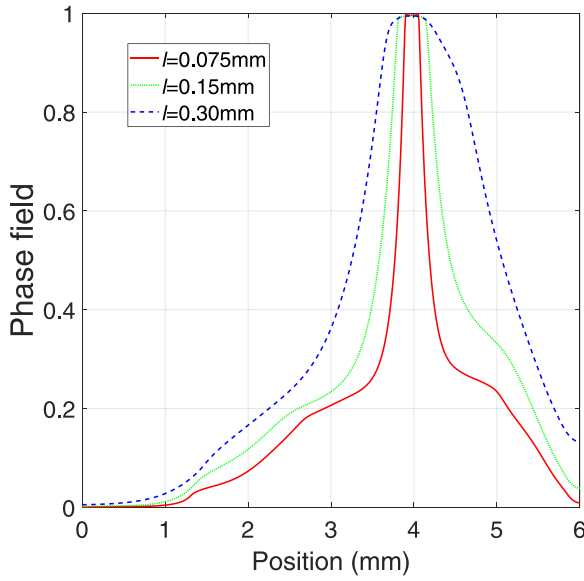


Fig. 9. The phase field with different ℓ 's at the time of complete fracture, $t = 1.62 \times 10^{-6}$ s.

Fig. 10 plots the evolution of the velocity at the left and right ends with different ℓ 's. As ℓ increases, three quantities of the right end decrease: the velocity drop to local minimum, the acceleration and the time required to reach local minimum, and vice versa for the left end.

Effect of the fracture energy release rate G_c . In this subsection, we change the value of G_c and keep the other parameters unchanged. We choose three values for G_c : 44 N/mm, 22 N/mm, and 11 N/mm. Fig. 11 plots the phase field with different G_c 's at $t = 1.62 \times 10^{-6}$ s. The complete fracture occurs at $t = 1.62 \times 10^{-6}$ s. The larger the G_c , the smaller the phase field at the same time and the same position. By comparing the results of varying G_c and ℓ , we find that these trends are very similar.

Fig. 12 plots the velocity of the left and the right end. As G_c decreases, the same three quantities of the right end decrease just as ℓ increases: the decrease in velocity to a local minimum, the acceleration, and the time required to reach local minimum, and vice versa for the left end.

Effect of the initial velocity v_0 . In this subsection, we change the value of v_0 and keep the other parameters unchanged. We choose three values for v_0 : 150 m/s, 503 m/s, and 5030 m/s. Fig. 13 plots the phase field with different v_0 's. At $v_0 = 150$ m/s, complete fracture does not occur

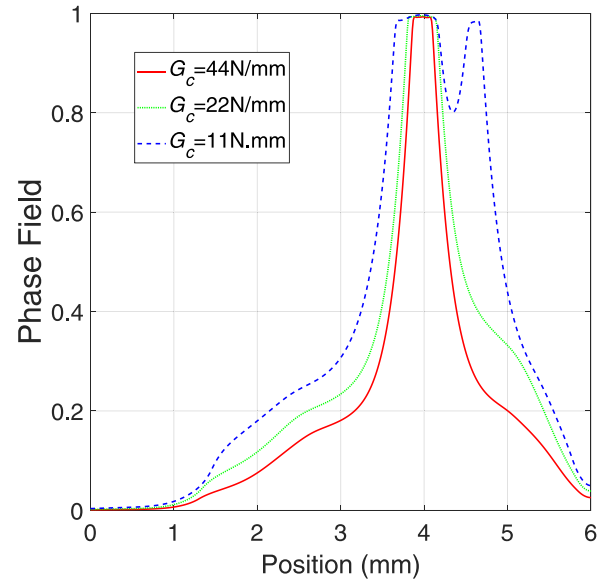
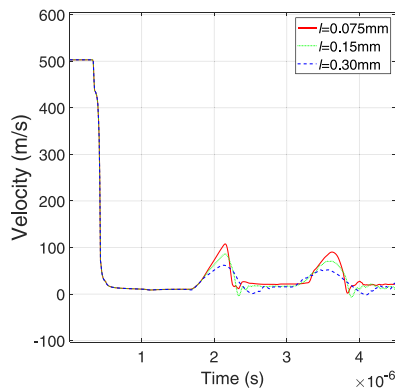


Fig. 11. The phase field with different G_c 's at the time of complete fracture, $t = 1.62 \times 10^{-6}$ s.

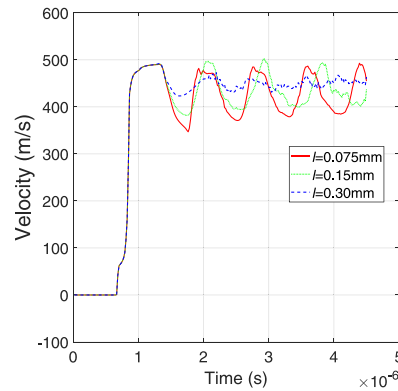
because there is not enough energy. When the two waves meet, the tensile stress is not enough to sustain the continuous increase of the phase field. The situation is the same as when G_c increases or when ℓ decreases. At $v_0 = 5030$ m/s, the length of the region where the phase field value finally reaches unity increases to about 1.5 mm. Complete fracture occurs at $t = 1.26 \times 10^{-6}$ s, much earlier than the example in Section 4.1.2.

Fig. 14 plots the velocity of the left and right ends with different v_0 's. The kinetic energy of the waves are mostly consumed to form the fracture; only a small part of kinetic energy is left and travel to the end nodes, which makes the left and right ends experience small vibrations. In summary, a larger ℓ , a smaller G_c , or a higher v_0 will increase the growth rate of the crack, as expected.

Effect of the Johnson-Cook parameter A . In this subsection, we change the value of A and keep the other parameters unchanged. We choose three values for A : 250 MPa, 496 MPa, and 1000 MPa. Fig. 15 plots the velocity of the left and right ends. As A increases, the jump of velocity at $t = 7 \times 10^{-7}$ s for the left end and at $t = 4 \times 10^{-7}$ s for the right end increases. For the left end, the increment to local maximum and the acceleration during the wave increases as A increases, and vice versa for the right end.



(a)



(b)

Fig. 10. Evolution of velocities of the left end (a) and right end (b) with different ℓ 's.

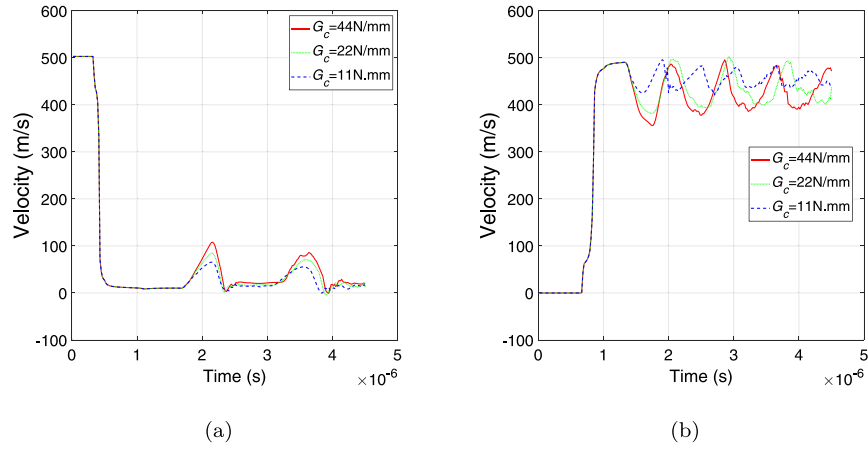


Fig. 12. Evolution of the velocity at the left end (a) and right end (b) with different G_c 's.

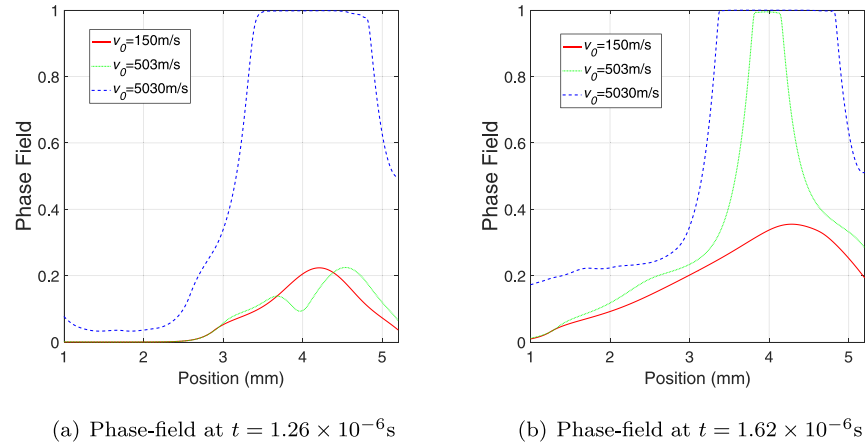


Fig. 13. Phase field growth with different v_0 's.

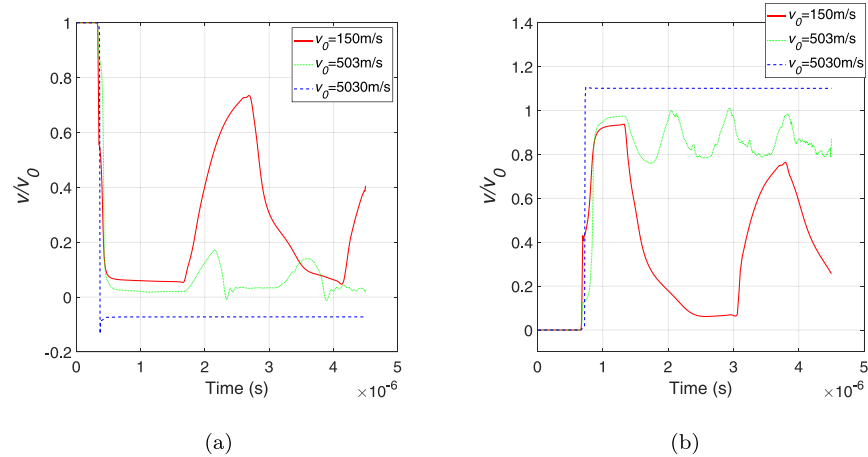


Fig. 14. Evolution of the velocity at the left end (a) and right end (b) with different v_0 's.

Effect of the Johnson-Cook parameter B . In this subsection, we change the value of B and keep the other parameters unchanged. We choose three values for B : 217 MPa, 434 MPa, and 868 MPa. Fig. 16 plots the velocity of the left and right ends with different B 's. As B increases,

three quantities of the right end increase: the decrease in velocity to a local minimum, the acceleration and the time required to reach local minimum, and vice versa for the left end. The effect of B is smaller compared to the other parameters we studied.

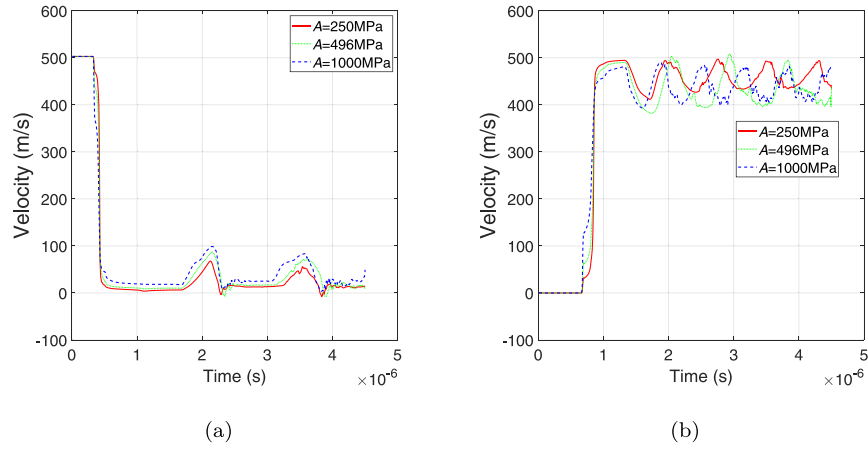


Fig. 15. Evolution of the velocity at the left end (a) and right end (b) with different A 's.

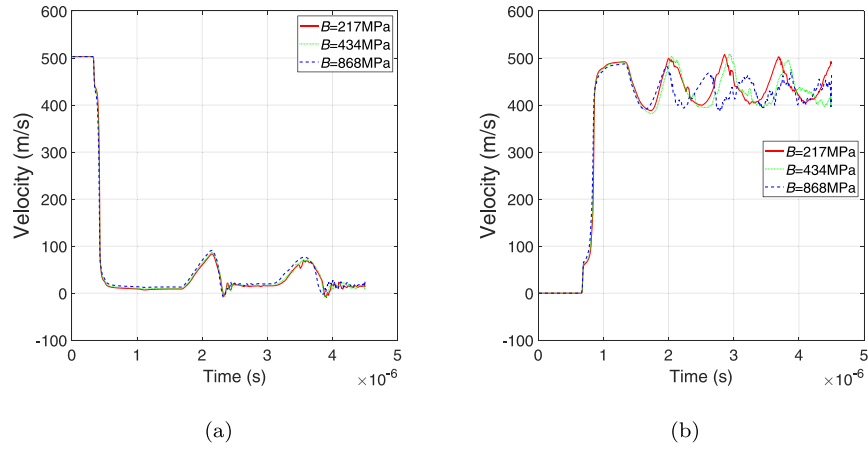


Fig. 16. Evolution of the velocity at the left end (a) and right end (b) with different B 's.

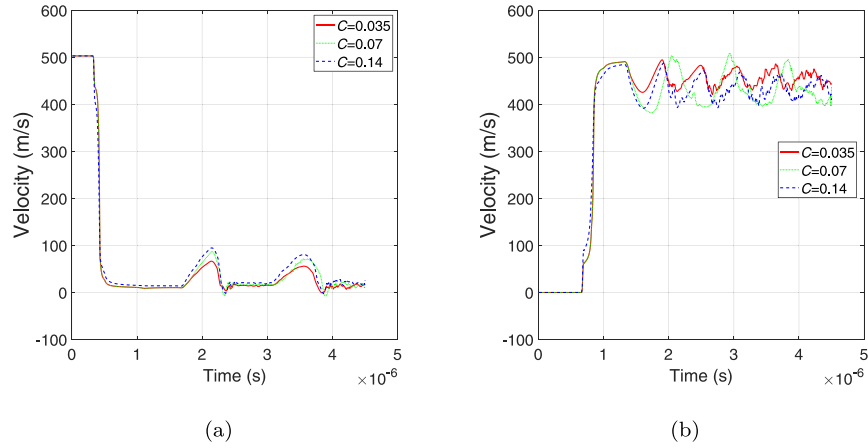


Fig. 17. Evolution of the velocity at the left end (a) and right end (b) with different C 's.

Effect of the Johnson-Cook parameter C . In this subsection, we change the value of C and keep the other parameters unchanged. We choose three values for C : 0.035, 0.07, and 0.14. Fig. 17 plots the velocity of the left and right ends. As C increases, the jump of velocity at $t = 7 \times 10^{-7}$ s for the left end and at $t = 4 \times 10^{-7}$ s for the right end increases. For the left end, the acceleration during the wave increases as C increases, and vice versa for the right end.

4.2. The split Hopkinson bar experiment on concrete

In this section, we conduct a numerical simulation on a split Hopkinson bar experiment as in [37]. Consider a bar $B_0^C = (0, L_3)$ made of wet concrete and a Hopkinson incident bar $B_0^I = (-L_2, 0)$ made of Al-alloy 6060-T5 with the same radius initially at rest and glued together. A striker bar $B_0^S = (-L_1 + L_2, -L_2)$ made of Al-alloy 6060-T5 with

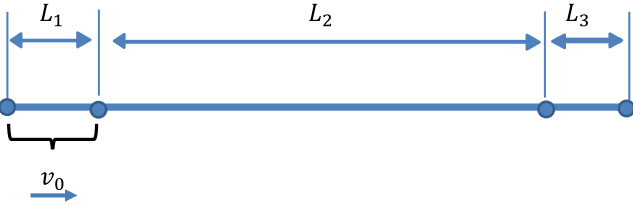


Fig. 18. The initial domain of the split Hopkinson bar experiment on concrete. The striker bar collides the incident bar with an impact velocity v_0 towards the right.

the same radius collides B_0^I along the normal direction at a velocity v_0 , as shown in Fig. 18. The initial domain is $B_0 = B_0^S \cup B_0^I \cup B_0^C$ and the impact interface is $X = -L_1$. The parameters used are listed in Table 2, which come from [37–40]. The other settings are the same as those in Section 4.1.

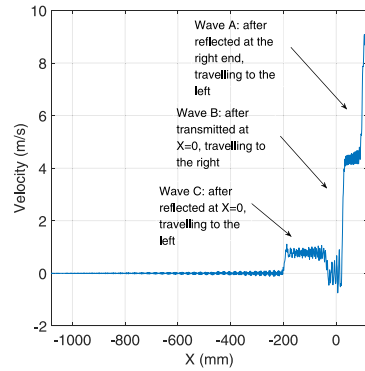
Fig. 19(a) and 19(b) plot the velocity as a function of the undeformed coordinate at the time just before the two waves meet and at the time of complete fracture, respectively. Fig. 19(c) and 19(d) plot the phase field and the equivalent plastic strain at the time of complete fracture. These figures reveal the whole process until fracture. Similar to the example in Section 4.1, two compression waves traveling to the right (Wave A) and to the left (Wave B) are produced right after the collision. These two waves become rarefaction waves after reflection

Table 2

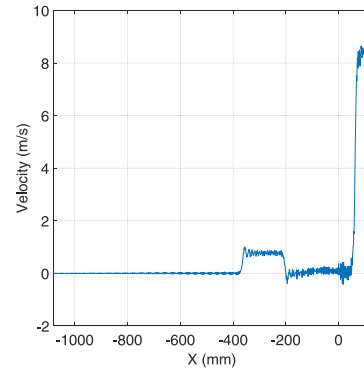
Material properties and parameters in the split Hopkinson bar experiment on concrete.

Parameter	Symbol	Value	Unit
Young's modulus of Al-alloy 6060-T5	E_1	69.5	GPa
Young's modulus of wet concrete	E_2	41.5	GPa
Poisson's ratio of Al-alloy 6060-T5	ν_1	0.32	–
Poisson's ratio of wet concrete	ν_2	0.21	–
Mass density of Al-alloy 6060-T5	ρ_1	2700	kg/m ³
Mass density of wet concrete	ρ_2	2340	kg/m ³
Critical energy release rate of Al-alloy 6060-T5	G_c^I	255	N/mm
Critical energy release rate of wet concrete	G_c^C	0.12	N/mm
Phase field regularized parameter of Al-alloy 6060-T5	ℓ_1	57	mm
Phase field regularized parameter of wet concrete	ℓ_2	34	mm
Johnson–Cook parameter of Al-alloy 6060-T5	A	240	MPa
Johnson–Cook parameter of Al-alloy 6060-T5	B	200	MPa
Johnson–Cook parameter of Al-alloy 6060-T5	C	0.05	–
Johnson–Cook parameter of Al-alloy 6060-T5	N	0.2	–
Yield strength of wet concrete	σ_s	4	MPa
Mesh size	h	1	mm
Time step	Δt	9×10^{-8}	s
Impact velocity	v_0	7	m/s
Length of striker bar B_0^S	L_1	80	mm
Length of incident bar B_0^I	L_2	1000	mm
Length of concrete specimen B_0^C	L_3	120	mm

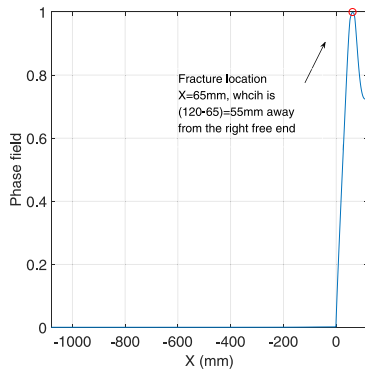
at the boundary. When and where they meet for the first time in the concrete, at about 60 mm away from the free end, a crack forms. The



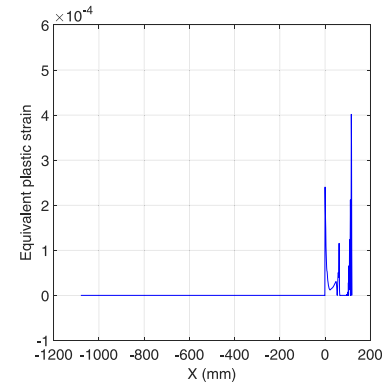
(a) Velocity as a function of the undeformed coordinate at $t = 1.97 \times 10^{-4}$ s (just before Wave A and Wave B meet)



(b) Velocity as a function of the undeformed coordinate at $t = 2.25 \times 10^{-4}$ s (at the time of the complete fracture)



(c) Phase field as a function of the undeformed coordinate at $t = 2.25 \times 10^{-4}$ s (at the time of the complete fracture)



(d) Equivalent plastic strain as a function of the undeformed coordinate at $t = 2.25 \times 10^{-4}$ s (at the time of the complete fracture)

Fig. 19. Velocity, phase field and equivalent plastic strain as a function of the undeformed coordinate before and after the fracture.

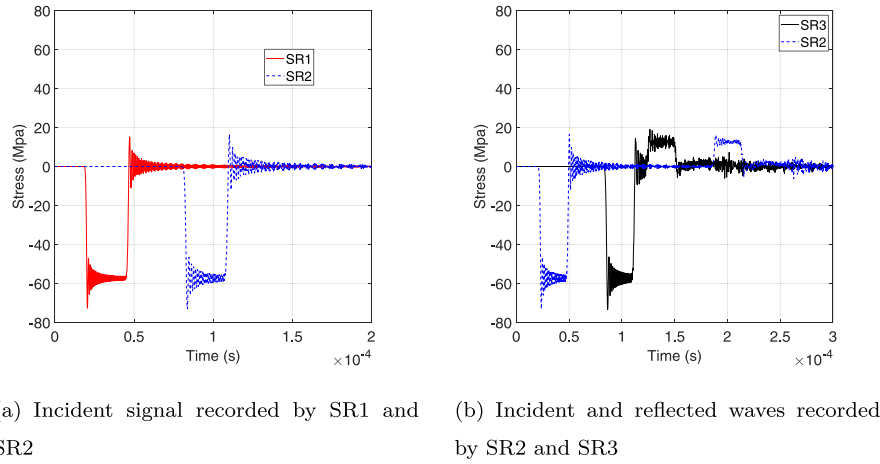


Fig. 20. Incident and reflected waves captured at the position of SR1, SR2 and SR3.

Table 3

Specified parameters and geometry parameters in the split Hopkinson bar experiment on aluminum alloy.

Parameter	Symbol	Value	Unit
Phase field regularized parameter of Al-alloy 6060-T5	ℓ_1	0.05	mm
Mesh size	h	0.01	mm
Time step	Δt	9×10^{-10}	s
Impact velocity	v_0	400	m/s
Length of striker bar B_0^S	L_1	2	mm
Length of incident bar B_0^I	L_2	2	mm
Length of aluminum specimen B_0^{Al}	L_3	1	mm
Length of transmitted bar B_0^T	L_4	1	mm
Radius of B_0^{Al}	r_1	0.5	mm
Radius of B_0^S , B_0^I , and B_0^T	r_2	3	mm

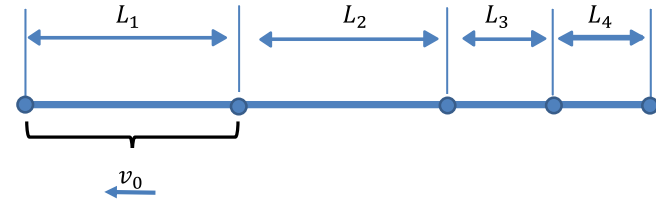


Fig. 21. The initial domains of the split Hopkinson bar on aluminum alloy. The striker bar stretches the incident bar with a velocity v_0 towards left.

phase field there continuously increases and finally reaches unity at

$t = 2.25 \times 10^{-4}$ s. It is worth noting that part of the wave reflected at the boundary between concrete and Al-alloy, namely Wave C, can be seen in Fig. 19(a).

In the experiment [37], three stress record stations, SR1, SR2, and SR3, are placed at 120 mm from the left end, midpoint and 120 mm from the right end of the B_0^{Al} , respectively. Fig. 20 plots the stresses at these positions from the numerical simulation. Compared with [37, Figure 6], the trends of stress evolution match well and the amplitudes are close to each other. From Fig. 19(c), we can see that the fracture location is about $X = 65$ mm, which is close to that recorded in the experiment, $X = 68$ mm.

4.3. The split Hopkinson bar experiment on aluminum alloy

In this section, we carry out another numerical simulation of the split Hopkinson bar experiment in [41]. Consider a bar $B_0^{Al} = (0, L_3)$ made of Al-alloy 6060-T5 with a radius r_1 , with an incident bar $B_0^I = (-L_2, 0)$ and a transmitted bar $B_0^T = (L_3, L_3 + L_4)$, both made of 45 steel with radius r_2 glued at the left and right ends. They are initially at rest. A striker bar $B_0^S = (-(L_1 + L_2), -L_2)$ made of 45 steel with radius r_2 glued to the left end of B_0^I leaves at a velocity v_0 , as shown in Fig. 21. The initial domain is $B_0 = B_0^S \cup B_0^I \cup B_0^{Al} \cup B_0^T$. The impact interface is $X = -L_2$. The parameters used are given in Table 1 and Table 2, unless specified in Table 3. The other settings are the same as in Section 4.1.

The stretch of B_0^S from B_0^I leads to two rarefaction waves, traveling to the left and to the right. Fig. 22 plots the velocity as a function of the undeformed coordinate before and at the time of fracture. Part

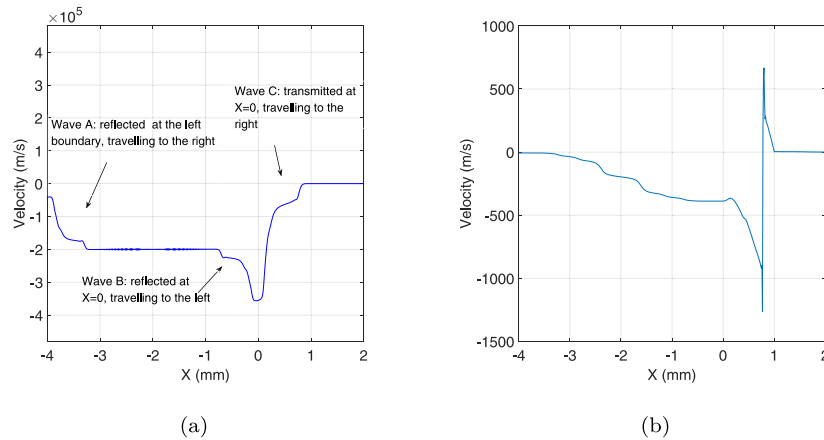


Fig. 22. Velocity as a function of the undeformed coordinate just after the wave reaches the boundary between B_0^I and B_0^S (a) and at the time of fracture (b).

of the wave is reflected, denoted as Wave B, while the rest, denoted as Wave C, continues propagating in B_0^{Al} . Since the linear density of B_0^{Al} is relatively small compared to the other parts, most of the waves are reflected at the boundary. Therefore, Wave C is standing in the specimen, continually stretches and finally leads to a fracture.

Fig. 23 plots the final phase field at $t = 9.56 \times 10^{-7}$ s, and the fracture location agrees well with the experimental result in [41], which again shows the effectiveness of the proposed model. Fig. 24 plots the equivalent plastic strain as a function of the undeformed coordinate at $t = 2.25 \times 10^{-4}$ s, and the maximal value appears at the fracture location $X = 0.77$ mm as expected.

5. Conclusions

In this paper, we propose a new phase field model in the updated Lagrangian framework for the shock wave problems, and the governing equation of phase field is reformulated in the deformed configuration. By incorporating the Johnson–Cook plasticity model using a return-mapping algorithm, we take into account both the strain hardening and strain rate hardening simultaneously. Besides, a new history variable is developed considering the tension–compression asymmetry to enforce the irreversibility condition of crack growth. Our simulation results agree well with experimental results on 45 steel and on two split Hopkinson bar experiments on concrete and aluminum alloy. Finally, a parameter study shows the correct trend of the simulation scheme, i.e., a larger regularization length scale ℓ , a smaller crack energy release rate G_c , or a higher initial velocity v_0 will increase the growth rate of the crack, as expected.

CRediT authorship contribution statement

Shourong Hao: Methodology, Software, Validation, Formal analysis, Investigation, Data curation, Writing – original draft, Writing – review & editing, Visualization. **Yihao Chen:** Software, Validation, Formal analysis, Investigation, Data curation, Writing – original draft, Writing – review & editing, Visualization. **Jun-Bo Cheng:** Conceptualization, Methodology, Resources, Supervision, Funding acquisition. **Yongxing Shen:** Conceptualization, Methodology, Resources, Writing – original draft, Writing – review & editing, Supervision, Project administration, Funding acquisition.

Declaration of competing interest

The authors declare that they have no known competing financial interests or personal relationships that could have appeared to influence the work reported in this paper.

Acknowledgments

This work is supported by the Science Challenge Project, China, No. TZ2016002, and by the National Natural Science Foundation of China, No. 12072043.

References

- [1] S. Li, W.-K. Liu, D. Qian, P.R. Guduru, A.J. Rosakis, Dynamic shear band propagation and micro-structure of adiabatic shear band, *Comput. Methods Appl. Mech. Engrg.* 191 (1–2) (2001) 73–92, [http://dx.doi.org/10.1016/S0045-7825\(01\)00245-6](http://dx.doi.org/10.1016/S0045-7825(01)00245-6).
- [2] S. Li, W.K. Liu, A.J. Rosakis, T. Belytschko, W. Hao, Mesh-free Galerkin simulations of dynamic shear band propagation and failure mode transition, *Int. J. Solids Struct.* 39 (5) (2002) 1213–1240, [http://dx.doi.org/10.1016/S0020-7683\(01\)00188-3](http://dx.doi.org/10.1016/S0020-7683(01)00188-3).
- [3] J.-H. Song, P.M. Areias, T. Belytschko, A method for dynamic crack and shear band propagation with phantom nodes, *Internat. J. Numer. Methods Engrg.* 67 (6) (2006) 868–893, <http://dx.doi.org/10.1002/nme.1652>.
- [4] X. Teng, T. Wierzbicki, H. Couque, On the transition from adiabatic shear banding to fracture, *Mech. Mater.* 39 (2) (2007) 107–125, <http://dx.doi.org/10.1016/j.mechmat.2006.03.001>.

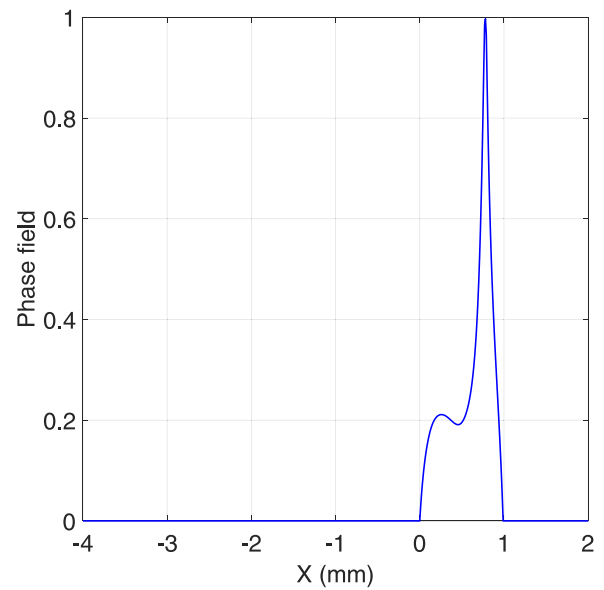


Fig. 23. Phase field as a function of the undeformed coordinate at the time of complete fracture, $t = 9.56 \times 10^{-7}$ s.

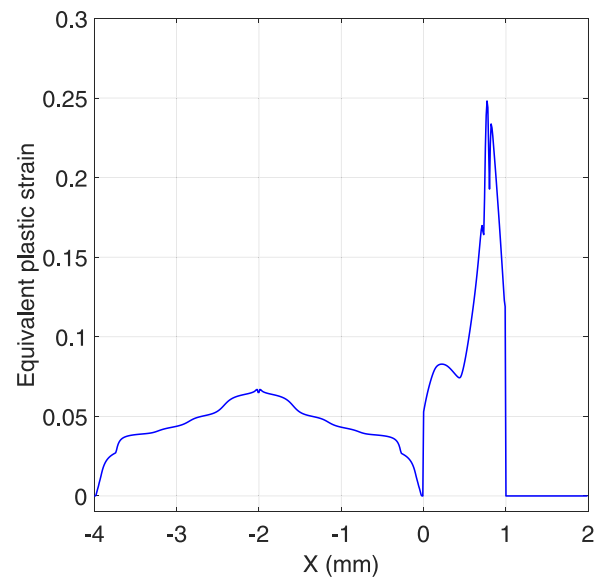


Fig. 24. Equivalent plastic strain as a function of the undeformed coordinate at the time of complete fracture, $t = 2.25 \times 10^{-4}$ s.

- [5] Y. Bao, T. Wierzbicki, On fracture locus in the equivalent strain and stress triaxiality space, *Int. J. Mech. Sci.* 46 (1) (2004) 81–98, <http://dx.doi.org/10.1016/j.ijmecsci.2004.02.006>.
- [6] W. Liu, G. Yang, Y. Cai, Modeling of failure mode switching and shear band propagation using the correspondence framework of peridynamics, *Comput. Struct.* 209 (2018) 150–162, <http://dx.doi.org/10.1016/j.compstruc.2018.08.007>.
- [7] B. Bourdin, G.A. Francfort, J.-J. Marigo, Numerical experiments in revisited brittle fracture, *J. Mech. Phys. Solids* 48 (4) (2000) 797–826, [http://dx.doi.org/10.1016/S0022-5096\(99\)00028-9](http://dx.doi.org/10.1016/S0022-5096(99)00028-9).
- [8] E. Samaniego, C. Anitescu, S. Goswami, V.M. Nguyen-Thanh, H. Guo, K. Hamdia, X. Zhuang, T. Rabczuk, An energy approach to the solution of partial differential equations in computational mechanics via machine learning: Concepts, implementation and applications, *Comput. Methods Appl. Mech. Engrg.* 362 (2020) 112790.

- [9] S. Goswami, C. Anitescu, S. Chakraborty, T. Rabczuk, Transfer learning enhanced physics informed neural network for phase-field modeling of fracture, *Theor. Appl. Fract. Mech.* 106 (2020) 102447.
- [10] M. Ambati, T. Gerasimov, L. De Lorenzis, A review on phase-field models of brittle fracture and a new fast hybrid formulation, *Comput. Mech.* 55 (2) (2015) 383–405, <http://dx.doi.org/10.1007/s00466-014-1109-y>.
- [11] J.-Y. Wu, V.P. Nguyen, C.T. Nguyen, D. Sutula, S. Sinaie, S.P. Bordas, Chapter One - Phase-field modeling of fracture, in: S.P.A. Bordas, D.S. Balint (Eds.), in: *Advances in Applied Mechanics*, vol. 53, Elsevier, 2020, pp. 1–183, <http://dx.doi.org/10.1016/bs.aams.2019.08.001>, URL <https://www.sciencedirect.com/science/article/pii/S0065215619300134>.
- [12] B. Bourdin, G.A. Francfort, Past and present of variational fracture, *SIAM News* 52 (9) (2019).
- [13] T. Wick, *Multiphysics Phase-Field Fracture: Modeling, Adaptive Discretizations, and Solvers*, vol. 28, Walter de Gruyter GmbH & Co KG, 2020.
- [14] S. Zhou, T. Rabczuk, X. Zhuang, Phase field modeling of quasi-static and dynamic crack propagation: COMSOL implementation and case studies, *Adv. Eng. Softw.* 122 (2018) 31–49, <http://dx.doi.org/10.1016/j.advengsoft.2018.03.012>.
- [15] V.P. Nguyen, J.-Y. Wu, Modeling dynamic fracture of solids with a phase-field regularized cohesive zone model, *Comput. Methods Appl. Mech. Engrg.* 340 (2018) 1000–1022, <http://dx.doi.org/10.1016/j.cma.2018.06.015>.
- [16] H. Ren, X. Zhuang, C. Anitescu, T. Rabczuk, An explicit phase field method for brittle dynamic fracture, *Comput. Struct.* 217 (2019) 45–56, <http://dx.doi.org/10.1016/j.compstruc.2019.03.005>.
- [17] T.K. Mandal, V.P. Nguyen, J.-Y. Wu, Evaluation of variational phase-field models for dynamic brittle fracture, *Eng. Fract. Mech.* 235 (2020) 107169, <http://dx.doi.org/10.1016/j.engfracmech.2020.107169>.
- [18] D. Chu, X. Li, Z. Liu, J. Cheng, T. Wang, Z. Li, Z. Zhuang, A unified phase field damage model for modeling the brittle-ductile dynamic failure mode transition in metals, *Eng. Fract. Mech.* 212 (2019) 197–209, <http://dx.doi.org/10.1016/j.engfracmech.2019.03.031>.
- [19] T. Wang, Z.L. Liu, Y.N. Cui, X. Ye, X.M. Liu, R. Tian, Z. Zhuang, A thermo-elastic-plastic phase-field model for simulating the evolution and transition of adiabatic shear band. Part I. Theory and model calibration, *Eng. Fract. Mech.* (2020) 107028, <http://dx.doi.org/10.1016/j.engfracmech.2020.107028>.
- [20] T. Wang, Z.L. Liu, Y.N. Cui, X. Ye, X.M. Liu, R. Tian, Z. Zhuang, A thermo-elastic-plastic phase-field model for simulating the evolution and transition of adiabatic shear band. Part II. Dynamic collapse of thick-walled cylinder, *Eng. Fract. Mech.* (2020) 107027, <http://dx.doi.org/10.1016/j.engfracmech.2020.107027>.
- [21] D. Grady, M. Kipp, The growth of unstable thermoplastic shear with application to steady-wave shock compression in solids, *J. Mech. Phys. Solids* 35 (1) (1987) 95–119, [http://dx.doi.org/10.1016/0022-5096\(87\)90030-5](http://dx.doi.org/10.1016/0022-5096(87)90030-5).
- [22] A. Molinari, Collective behavior and spacing of adiabatic shear bands, *J. Mech. Phys. Solids* 45 (9) (1997) 1551–1575, [http://dx.doi.org/10.1016/S0022-5096\(97\)00012-4](http://dx.doi.org/10.1016/S0022-5096(97)00012-4).
- [23] T. Wright, H. Ockendon, A scaling law for the effect of inertia on the formation of adiabatic shear bands, *Int. J. Plast.* 12 (7) (1996) 927–934, [http://dx.doi.org/10.1016/S0749-6419\(96\)00034-4](http://dx.doi.org/10.1016/S0749-6419(96)00034-4).
- [24] Z. Lovinger, D. Rittel, Z. Rosenberg, An experimental study on spontaneous adiabatic shear band formation in electro-magnetically collapsing cylinders, *J. Mech. Phys. Solids* 79 (2015) 134–156, <http://dx.doi.org/10.1016/j.jmps.2015.04.007>.
- [25] Z. Lovinger, D. Rittel, Z. Rosenberg, Modeling spontaneous adiabatic shear band formation in electro-magnetically collapsing thick-walled cylinders, *Mech. Mater.* 116 (2018) 130–145, <http://dx.doi.org/10.1016/j.mechmat.2017.01.010>.
- [26] T. Brepols, I.N. Vladimirov, S. Reese, Numerical comparison of isotropic hypo- and hyperelastic-based plasticity models with application to industrial forming processes, *Int. J. Plast.* 63 (2014) 18–48, <http://dx.doi.org/10.1016/j.ijplas.2014.06.003>.
- [27] J.C. Simo, T.J.R. Hughes, *Computational Inelasticity*, Springer Verlag, New York, 1998, <http://dx.doi.org/10.1007/b98904>.
- [28] C. McAuliffe, H. Waisman, On the importance of nonlinear elastic effects in shear band modeling, *Int. J. Plast.* 71 (2015) 10–31, <http://dx.doi.org/10.1016/j.ijplas.2015.04.004>.
- [29] C. McAuliffe, H. Waisman, A unified model for metal failure capturing shear banding and fracture, *Int. J. Plast.* 65 (2015) 131–151, <http://dx.doi.org/10.1016/j.ijplas.2014.08.016>.
- [30] C. McAuliffe, H. Waisman, A coupled phase field shear band model for ductile–brittle transition in notched plate impacts, *Comput. Methods Appl. Mech. Engrg.* 305 (2016) 173–195, <http://dx.doi.org/10.1016/j.cma.2016.02.018>.
- [31] M.J. Borden, T.J.R. Hughes, C.M. Landis, A. Anvari, I.J. Lee, A phase-field formulation for fracture in ductile materials: Finite deformation balance law derivation, plastic degradation, and stress triaxiality effects, *Comput. Methods Appl. Mech. Engrg.* 312 (2016) 130–166, <http://dx.doi.org/10.1016/j.cma.2016.09.005>.
- [32] M. Ambati, R. Kruse, L. De Lorenzis, A phase-field model for ductile fracture at finite strains and its experimental verification, *Comput. Mech.* 57 (1) (2016) 149–167, <http://dx.doi.org/10.1007/s00466-015-1225-3>.
- [33] G.R. Johnson, W.H. Cook, A constitutive model and data for metals subjected to large strains, high strain rates and high temperatures, *Proceedings of the 7th International Symposium on Ballistics*, vol. 21, The Netherlands, 1983, pp. 541–547.
- [34] C. Miehe, M. Hofacker, F. Welschinger, A phase field model for rate-independent crack propagation: Robust algorithmic implementation based on operator splits, *Comput. Methods Appl. Mech. Engrg.* 199 (45–48) (2010) 2765–2778, <http://dx.doi.org/10.1016/j.cma.2010.04.011>.
- [35] M. Dowell, P. Jarratt, The “Pegasus” method for computing the root of an equation, *BIT Numer. Math.* 12 (4) (1972) 503–508, <http://dx.doi.org/10.1007/BF01932959>.
- [36] C.-M. Hu, H.-L. He, S.-S. Hu, Research on the spalling of 45# steel under different strain rate, *J. Exp. Mech.* 18 (2) (2003) 246–250, <http://dx.doi.org/10.3969/j.issn.1001-4888.2003.02.018>.
- [37] J. Klepaczk, A. Brara, An experimental method for dynamic tensile testing of concrete by spalling, *Int. J. Impact Eng.* 25 (4) (2001) 387–409, [http://dx.doi.org/10.1016/S0734-743X\(00\)00050-6](http://dx.doi.org/10.1016/S0734-743X(00)00050-6).
- [38] X. Fan, T. Suo, Q. Sun, T. Wang, Dynamic mechanical behavior of 6061 Al alloy at elevated temperatures and different strain rates, *Acta Mech. Solida Sin.* 26 (2) (2013) 111–120, [http://dx.doi.org/10.1016/S0894-9166\(13\)60011-7](http://dx.doi.org/10.1016/S0894-9166(13)60011-7).
- [39] J.-Y. Wu, A unified phase-field theory for the mechanics of damage and quasi-brittle failure, *J. Mech. Phys. Solids* 103 (2017) 72–99, <http://dx.doi.org/10.1016/j.jmps.2017.03.015>.
- [40] L.D.L. Marreddy Ambati, A phase-field model for ductile fracture at finite strains and its experimental verification, *Comput. Mech.* 57 (2016) 149–167, <http://dx.doi.org/10.1007/s00466-015-1225-3>.
- [41] Z. Jiang, M. Xing, Y. Wang, Experimental study on dynamic tensile failure of selected aluminum alloys, *Chinese J. Solid Mech.* 35 (6) (2014) 552–558.